Scientific Research Publishing

Advances in Aerospace Science and Technology, 2026, 11(1), 1-19
https://www.scirp.org/journal/aast
ISSN Online: 2473-6724
ISSN Print: 2473-6708

# Study on Aerodynamic Interference in Helicopter Mode of a Tiltwing Aircraft

**Wentong Deng, Yun Peng, Guoyi He, Xinxin Ouyang, Binghua Xie**

Department of Aeronautics and Astronautics, Nanchang Hangkong University, Nanchang, China
Email: 34016@nchu.edu.cn

**How to cite this paper:** Deng, W.T., Peng, Y., He, G.Y., Ouyang, X.X. and Xie, B.H. (2026) Study on Aerodynamic Interference in Helicopter Mode of a Tiltwing Aircraft. *Advances in Aerospace Science and Technology*, **11**, 1-19.
https://doi.org/10.4236/aast.2026.111001

**Received:** February 9, 2026
**Accepted:** March 13, 2026
**Published:** March 16, 2026



## Abstract

Tiltwing aircraft achieve the transition between helicopter mode and cruise mode through the synchronous tilting of the wing and rotors, thereby combining vertical takeoff and landing capability with high-speed cruise performance. However, in helicopter mode, pronounced aerodynamic interference exists between the rotor wake and the wing, which adversely affects the overall aerodynamic performance of the aircraft. In this study, an unsteady numerical simulation methodology applicable to tiltwing aircraft operating in helicopter mode is established, with particular emphasis on investigating the effectiveness of flaperon deflection in alleviating such aerodynamic interference. The results indicate that appropriate flaperon deflection can mitigate the aerodynamic interaction between the wing and the rotor. Nevertheless, the flaperon deflection rate has a significant influence on the evolution of hub vortex structures; excessively high deflection rates may lead to vortex breakdown and anomalous pressure distributions, thereby degrading the effectiveness of flaperon deflection. The findings of this study provide useful guidance for selecting suitable flaperon deflection simulation strategies during the vertical takeoff and landing phase of tiltwing aircraft.

## Keywords

Tiltwing, Helicopter Mode, Remeshing, Momentum Source, Flaperon

## 1. Introduction

In recent years, the global agenda for carbon neutrality has accelerated, while urban congestion and regional transportation bottlenecks have become increasingly severe. Against this backdrop, electric vertical take-off and landing (eVTOL) aircraft have rapidly evolved from proof-of-concept demonstrators to a new focal point of industrial competition [1]. Their runway-independent operation, low

acoustic footprint, and highly redundant three-dimensional maneuvering capability enable, for the first time, the conditions necessary for scalable point-to-point aerial transportation. On the uncrewed side, eVTOL platforms have been deeply integrated into scenarios, such as emergency logistics, maritime inspection, and high-rise firefighting [2] [3]. For crewed applications, concurrent breakthroughs in high-energy-density batteries, distributed electric propulsion, civil-aviation-grade flight control systems, and lightweight composite structures have enabled multi-passenger demonstrators to progressively complete flight testing and airworthiness assessments. Urban air mobility (UAM) is therefore approaching the threshold of commercialization. As a new generation of aircraft, eVTOL vehicles are experiencing transformative growth within the UAM domain and are widely regarded as potential primary carriers for future urban aerial commuting [4]-[6].

Compared with multirotor and lift-plus-cruise configurations, tiltwing concepts exhibit pronounced differences in overall aerodynamic layout and performance emphasis. Multirotor aircraft employ a purely rotor-borne aerodynamic architecture with relatively simple system composition. Such configurations impose minimal requirements on takeoff and landing infrastructure and are well suited for operations in complex environments [7]-[9]. However, because lift is generated entirely by the rotors, the cruise lift-to-drag ratio is typically low, resulting in limited forward speed and reduced range. In addition, multirotor systems demand a high level of coordination among rotors and motors; failure of a single rotor can readily induce attitude instability or even loss of control. Lift-plus-cruise configurations achieve vertical takeoff and landing through dedicated lifting rotors, while a fixed wing provides the majority of lift during cruise. Nevertheless, these aircraft generally carry two relatively independent propulsion and lift systems. The lifting rotors remain idle in cruise, constituting significant dead weight and additional parasitic drag, thereby degrading aerodynamic efficiency. Tiltwing aircraft, by contrast, realize synchronous rotation of the propulsion system together with portions of the wing structure, effectively reducing the download acting on the wing [10]. This approach mitigates the dead-weight penalty while retaining the high cruise speed and long-range advantages associated with wing-borne flight.

However, owing to the unique tiltwing configuration, the aerodynamic characteristics of tiltwing aircraft during the conversion phase are highly complex. In particular, in helicopter mode, strong aerodynamic coupling between the rotor wake and the airframe can induce attitude instabilities, posing significant challenges to the design of the flight control system. Therefore, a systematic investigation of the aerodynamic interference characteristics of tiltwing aircraft in helicopter mode is of substantial theoretical importance and engineering relevance.

Extensive and systematic investigations have been conducted by both domestic and international researchers on the aerodynamic interference between wings and rotors. These studies span multiple levels of fidelity and primarily employ two methodological approaches: experimental investigations and numerical simula-

tions. In terms of experimental research, wind tunnel testing has served as the primary platform for physically reproducing tiltwing aircraft configurations under full operational modes and a wide range of attitudes. Maisel [11] was the first to establish a publicly accessible, "full-scale" hover performance benchmark for tiltwing aircraft, which subsequently became a direct reference for power-payload and noise certification requirements of aircraft such as the V-22 and AW609. This work also formalized the standard tiltwing testing methodology combining flight-test force balances with onboard telemetry systems. Felker [12] was the first to experimentally demonstrate that the "blade-tip vortex-wing trailing-edge" interaction in hover is a primary source of power losses and high-frequency vibrations in tiltwing aircraft, providing quantitatively validated evidence that directly informed design refinements of the V-22 as well as subsequent noise and vibration mitigation standards. With respect to numerical simulations, benefiting from the rapid advances in high-performance computing (HPC) architectures and parallel algorithms over the past two decades, computational fluid dynamics (CFD) has emerged as a core tool for investigating the aerodynamic characteristics of tiltwing aircraft. Li Peng [13] demonstrated, using CFD techniques, that the aerodynamic interference between the wing and rotors in hover has a significant impact on overall aerodynamic performance. Wang Zonghui *et al.* [14] [15] employed an improved delayed detached-eddy simulation (DDES) approach to compute and analyze the aerodynamic interference flow field of a tiltwing aircraft, revealing that the characteristics of rotor-induced interference on the wing vary markedly across different stages of the tilt transition. Although traditional high-fidelity CFD methods are capable of accurately resolving complex flow physics, they are generally associated with long computational times and high computational costs. Consequently, many researchers have adopted momentum-source models to replace explicitly resolved propellers or rotors, enabling steady-state simulations of tiltwing aircraft during vertical takeoff and landing as well as during the tilt-transition phase [16].

To date, extensive systematic studies on tiltwing aircraft and their derivative configurations have been conducted both domestically and internationally, encompassing theoretical analyses, wind tunnel experiments, and numerical simulations in helicopter mode, transition mode, and fixed-wing mode. These efforts have preliminarily elucidated the global aerodynamic characteristics and flow mechanisms of tilt-type aircraft across the full flight envelope, providing important theoretical foundations and methodological support for overall aerodynamic layout optimization and flight control system design. However, existing studies and publicly available databases are predominantly focused on pure tiltwing or pure tiltwing configurations, while comparatively limited attention has been devoted to the aerodynamic characteristics and flight performance of tiltwing aircraft operating in helicopter mode. Consequently, further in-depth investigations in this area remain necessary.

To enhance the flight performance of tilt-wing aircraft in helicopter mode, ex-

isting studies have primarily focused on improving tilt strategies and rotor speed allocation methods to achieve better handling qualities. However, investigations into the role of wing-mounted control surfaces remain relatively limited. Flaperons, as critical aerodynamic components that integrate both lift augmentation and attitude control functions, can generate precise roll, pitch, and yaw moments through differential deflection, thereby enabling rapid attitude response and stable control. In helicopter mode, flaperons can also effectively regulate flow separation and pressure distribution over the wing surface, which is of significant importance for improving takeoff and landing safety.

This study employs a mesh reconstruction technique and develops a numerical methodology for effectively simulating the helicopter mode of a tilt-wing aircraft based on the Navier-Stokes (N-S) equations augmented with momentum source terms. The mesh reconstruction approach is utilized to accurately represent the kinematic motion of the flaperon surfaces, while the physical rotor blades are modeled using distributed momentum source terms. This strategy enables effective capture of rotor wake characteristics while maintaining computational efficiency and cost control.

## 2. Numerical Simulation Method and Grid Model

### 2.1. Flow Control Equations and Momentum Source Method

In the present study, the governing differential equations are discretized using the finite volume method, and the $k-\omega$ shear stress transport (SST) turbulence model is employed to account for turbulent effects. The governing equations consist of the three-dimensional incompressible Reynolds-averaged Navier-Stokes (RANS) equations, in which a momentum source term is incorporated. In accordance with the assumptions adopted in this investigation, the effects of body forces and heat conduction are neglected:

$$\frac{\partial}{\partial t}\int_{v} \boldsymbol{W} dv + \int_{\partial v} \left(\boldsymbol{F}_c - \boldsymbol{F}_v\right) ds = \int_{v} \boldsymbol{S} dv \,. \tag{1}$$

In Equation (1), $\boldsymbol{W}$ represents the variable for conservation of flow field, $\boldsymbol{F}_c$ represents the convection flux, $\boldsymbol{F}_v$ represents the viscous flux, $\boldsymbol{S}$ represents the source item, $v$ represents the volume of the control body element, $dv$ represents the surface of the control body element, $ds$ represents the area of the control body element.

The momentum source method replaces the physical blade geometry with a virtual actuator disk model. The aerodynamic forces exerted by the blades on the surrounding flow are transformed into equivalent momentum source terms, which are incorporated into the governing equations and solved in a coupled manner with the flow field. Let the Cartesian coordinate system of the computational domain be defined as O-XYZ, and the Cartesian coordinate system attached to the rotor disk be defined as O-XYZ. The transformation relationship between these two coordinate systems can be expressed as follows:

$$\begin{bmatrix} \xi \\ \eta \\ \zeta \end{bmatrix} = \begin{bmatrix} \cos\beta_{1c} & \sin\beta_{1s}\sin\beta_{1c} & -\sin\beta_{1s}\sin\beta_{1c} \\ 0 & \cos\beta_{1s} & \sin\beta_{1s} \\ \sin\beta_{1c} & -\sin\beta_{1s}\cos\beta_{1c} & \cos\beta_{1s}\cos\beta_{1c} \end{bmatrix} \times \begin{bmatrix} x - x_c \\ y - y_c \\ z - z_c \end{bmatrix} \tag{2}$$

In the above formulation, $\beta_{1s}$ and $\beta_{1c}$ denote the rotor disk roll (lateral tilt) angle and pitch (longitudinal tilt) angle, respectively. When the vehicle operates in helicopter mode, both angles are equal to zero. The vector $(x_c, y_c, z_c)$ represents the coordinates of the rotor disk center in the Cartesian coordinate system of the computational domain.

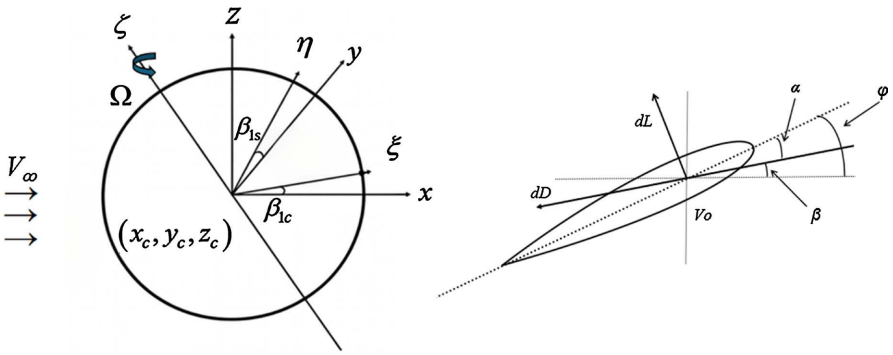


**Figure 1.** Schematic of the rotor disk coordinate system and the blade micro-tip segment.

In the derivation of the momentum source terms, a blade element differential segment of spanwise length dr is extracted along the blade radial direction. An infinitesimal blade element located at radius r, with chord length c and azimuth angle $\psi$, is considered for analysis, as illustrated in **Figure 1**. According to Newton's third law, the force acting on an infinitesimal blade element implies an equal and opposite force exerted by that blade element on the fluid. Therefore, the force applied to the airflow at the location of the blade element per unit time can be expressed as:

$$S'_{\Delta} = N \cdot dF' \cdot \frac{\Delta\psi}{\Omega} \cdot \frac{\Omega}{2\pi} = N \cdot dF' \cdot \frac{\Delta\psi}{2\pi} \tag{3}$$

In Equation (2),where $S^*_{\Delta}$ denotes the momentum source term; N is the number of blades of the propeller; $\Omega/2\pi$ represents the angular displacement per unit time; and $\Delta\psi/\Omega$ is the time required for the rotation. By transforming $S^*_{\Delta}$ into the computational-domain coordinate system $(x, y, z)$, the corresponding momentum source term $(S_x, S_y, S_z)$ can be obtained.

## 2.2. Momentum Source Method Example Verification

The rotor in helicopter mode was numerically simulated using the momentum source method. The dynamic pressure distributions were monitored at two radial stations located at 0.215R and 0.660R from the rotor center, where R denotes the rotor radius. The computed results were compared with the experimental data reported in Ref. [17]. The comparison is presented in **Figure 2**. As shown in the figure, the dynamic pressure distributions predicted by the momentum source

method agree well with the experimental trends, thereby demonstrating the validity and reliability of the present computational approach.

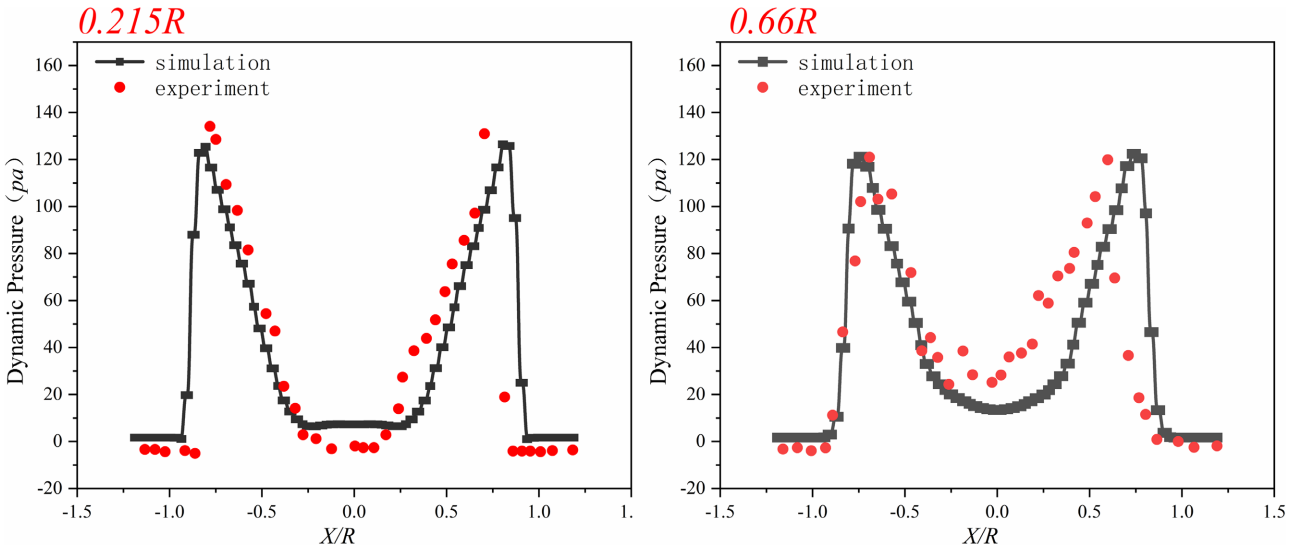


**Figure 2.** The comparison chart of the dynamic pressure distribution beneath the rotor.

## 2.3. Computational Model and Mesh Generation

To investigate the aerodynamic interference characteristics of a tiltwing aircraft operating in helicopter mode, the geometric model of the vehicle is first established, as shown in Figure 3. The geometric configurations of the aircraft under three distinct operating modes are presented. The aircraft adopts a twin-propeller tiltwing configuration, with the propellers mounted on the tilting wing segments.

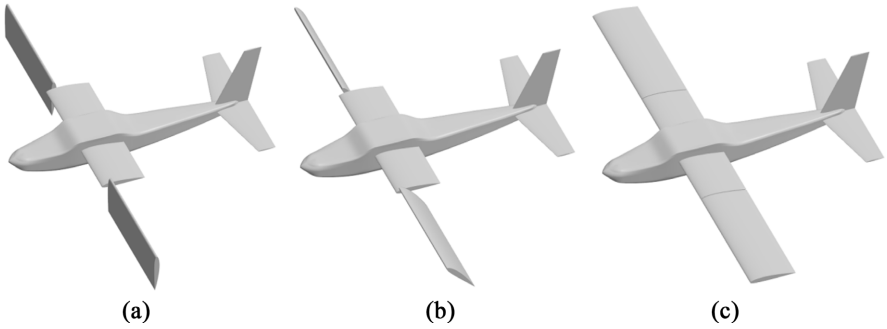


**Figure 3.** Geometric models of a tiltwing aircraft in three flight modes. (a) Helicopter Mode; (b) Tilting Transition Mode; (c) Fixed-Wing Mode.

This study focuses on the aerodynamic interference characteristics between the wing's tilt segment and the rotor in a tilt-rotor aircraft. To eliminate the influence of geometric parameters such as the upward sweep angle and root-taper ratio on the results, the wing is modeled using the simplest configuration-a rectangular, straight wing. In order to reduce computational complexity and emphasize the primary research focus, the aerodynamic coupling effects between the aircraft's fuselage, horizontal tail, and the wing-rotor system are not considered in this

study. Additionally, the effects of lateral-directional forces are neglected. Therefore, the computational model is simplified to include only a single wing and the rotor. The specific parameters are provided in Table 1.

Table 1. Wing modeling parameters.

| Parameter | Data | Parameter | Data |
|---|---|---|---|
| Wing airfoil | NACA 4412 | Blade airfoil | VR-5 |
| Wingspan of a fixed-wing segment (m) | 6 | Rotor radius (m) | 1.35 |
| Wingspan of a tilt-wing Segment (m) | 6 | Rotor root chord length(m) | 0.131 |
| Wing chord length (m) | 1 | Rotor tip chord length(m) | 0.074 |
| Rotor hub radius (m) | 0.2514 | Number of blades | 5 |
| Horizontal vertical tail airfoil | NACA 0015 | Flat tail extension | 4.5 |

Since the propeller is represented using the momentum source method, explicit geometric modeling of the propeller is not required. Instead, a locally refined mesh region is generated at the propeller location. This region is defined as a cylindrical volume with a radius of 1.35 m and a height of 0.2 m. Figure 4 presents the front view of the wing model used in the numerical simulations.

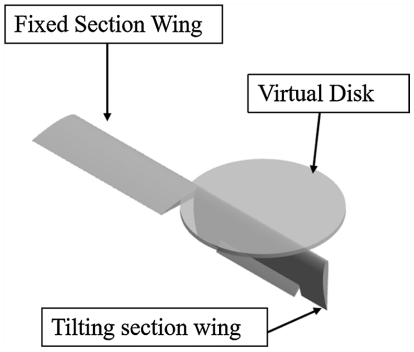


Figure 4. Wing model main view.

The entire flow field computational domain is a rectangular region with dimensions of 90 m × 90 m × 45 m. The inlet is defined as a velocity inlet, while the outlet is set as a pressure outlet. The wing root plane is designated as the symmetry plane, and the wing surface is treated as a wall. The remaining boundaries are set as symmetry planes. The distribution of these boundary conditions is illustrated in Figure 5.

## 2.4. Grid Independence Verification

A non-structured (unstructured) mesh is employed to discretize the computational domain. Mesh motion techniques are utilized to simulate the deflection process of the flaperon, and a conventional mesh remeshing trigger is imple-

mented such that predefined mesh operations are automatically executed when the mesh quality falls below specified criteria. To more accurately resolve the near-wall flow over the wing surface, prism layer meshes are generated along the wing surface, with the height of the first layer set to $2.40668 \times 10^{-5}$ m. A total of 22 prism layers are applied, with a growth ratio of 1.3. Figure 6 presents the sectional meshes of the wing and the rotor, respectively.

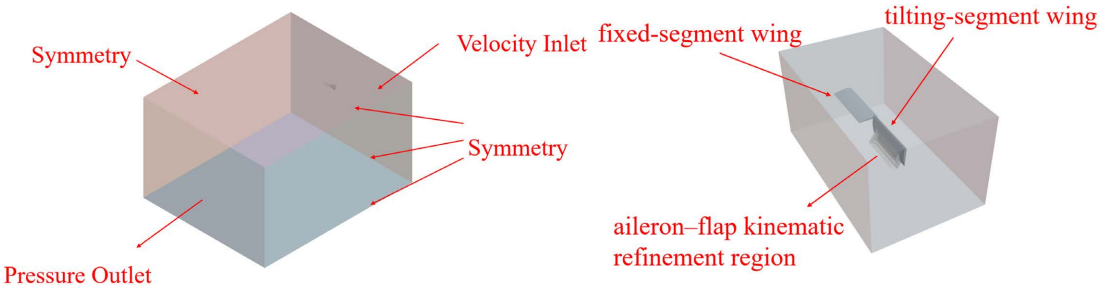


**Figure 5.** Computational domain.

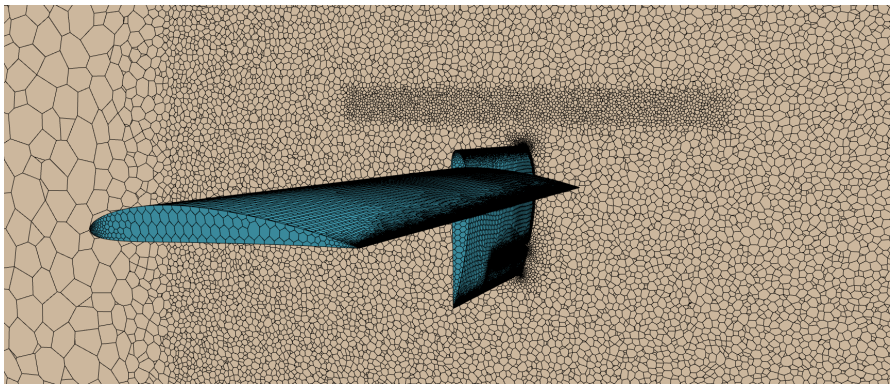

**Figure 6.** Grid view.

A grid independence study is a critical step to ensure the accuracy and reliability of numerical simulation results. Both grid quality and grid resolution have a significant influence on computational accuracy and efficiency. To assess the effect of grid discretization on the numerical results, multiple computational grids with varying levels of refinement were generated. Numerical simulations were conducted for each grid under identical boundary conditions, followed by a comparative analysis of the results.

The computational boundary conditions were specified as follows: the freestream velocity was set to 5 m/s, the propeller rotational speed was 1500 RPM, and the flaperon deflection angle was 0˚. The thrust generated by the rotor is denoted as *T*. Under the influence of the rotor wake, the wing experiences both horizontal and vertical aerodynamic forces. The horizontal force acting on the wing is denoted as $F_x$, defined as positive along the negative direction of the body-fixed x-axis. The vertical force on the wing is represented by *Fz*, defined as positive along the negative direction of the body-fixed y-axis. The numerical results obtained with different grid resolutions are presented in Figure 7. As shown in the figure,

the ratio $Fz/T$ increases with increasing grid resolution and approaches convergence when the total number of grid cells exceeds 7.18 million. Considering both the accuracy of the numerical results and the computational cost, the grid containing 7.18 million cells was selected for the simulations presented in this study.

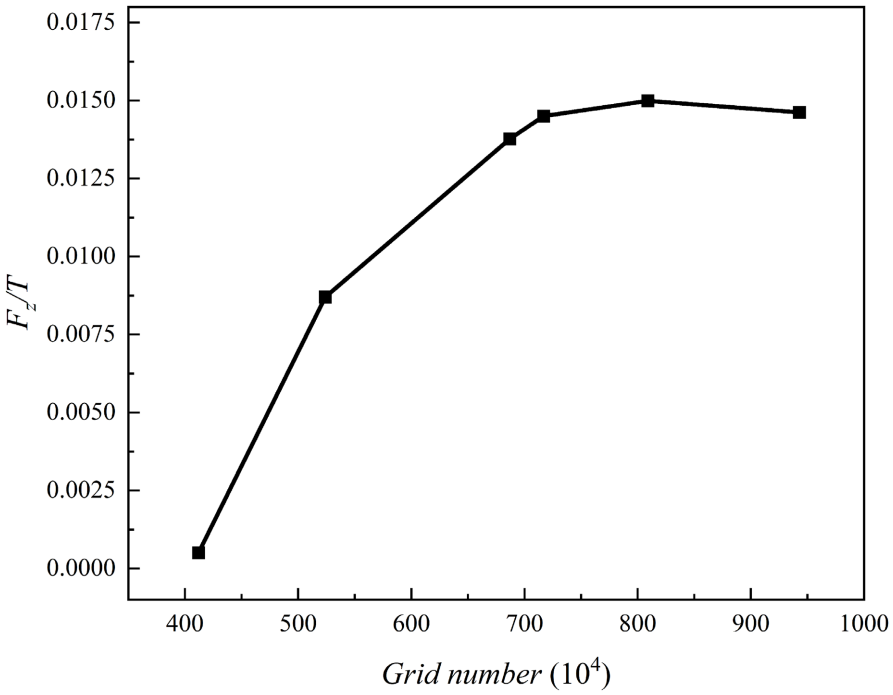


**Figure 7.** Grid independence verification.

## 3. Study on the Aerodynamic Interference Characteristics of Rotor-Wing Interaction in the Tilt Phase under Different Inflow Conditions

### 3.1. Steady-State Computational Conditions

The definition of the tilt angle of a tiltwing aircraft is based on the flight mode: a tilt angle of 0˚ corresponds to the fixed-wing mode, while 90˚ corresponds to the helicopter mode. In the helicopter mode, the angle between the wing chord line and the fuselage longitudinal axis is set to 4˚, so that the thrust direction generated by the rotors is aligned with the direction corresponding to the zero-lift angle of attack of the tiltwing. This configuration effectively reduces the aerodynamic interference of the rotors on the wing in the tilting segment [18]. Therefore, in the present study, the tilt angle of the wing is set to 86˚.

To investigate the aerodynamic interaction between the wing in the tilting segment and the rotors under varying inflow velocities, the freestream velocity at the inlet is prescribed as constant and set to 0 m/s, 1 m/s, and 2 m/s, respectively, while the angle of attack of the fixed-wing segment is maintained at 0˚. The rotor rotational speed is fixed at 1500 RPM, and the flaperons are kept undeflected. The detailed computational cases are summarized in Table 2.

**Table 2.** Computational conditions for studying the effects of different freestream velocities.

| Parameters | Value |
|---|---|
| Freestream velocity (m/s) | 0 - 8 |
| Fixed-wing angle of attack(deg) | 0 |
| Rotor and tilt-wing segment angle (deg) | 86 |
| Rotor rotation speed (RPM) | 1500 |
| Flaperon deflection angle (deg) | 0 |

### 3.2. Steady-State Computational Results

Figure 8 illustrates the variation of aerodynamic loads on the tilt-segment wing as a function of inflow velocity (where $F_x$ denotes the force in the horizontal direction, $Fz$ the force in the vertical direction, and V the inflow velocity). The computational results indicate that, under the influence of rotor wake, both the fixed-segment wing and the tilt-segment wing experience a vertical force $Fz$ and a horizontal force $F_x$. However, the fixed-segment wing is located far from the core region of the rotor wake and is therefore subjected to relatively weak aerodynamic interference, which can be neglected. For the tilt-segment wing, a pronounced coupling with the rotor wake is observed. As shown in Figure 8(a), with increasing inflow velocity, the ratio of the horizontal force $F_x$ to the rotor thrust T increases monotonically.

Owing to the relatively small projected area of the tilt-segment wing in the xy-plane, its blockage effect on the rotor wake is limited. As shown in Figure 8(b), the ratio of the vertical force $Fz$ to the rotor thrust T also increases with increasing inflow velocity; however, its magnitude does not exceed 0.2% of the total rotor thrust. Consequently, this vertical force has a negligible influence on the investigation of aerodynamic interference between the wing and the rotor. Based on the

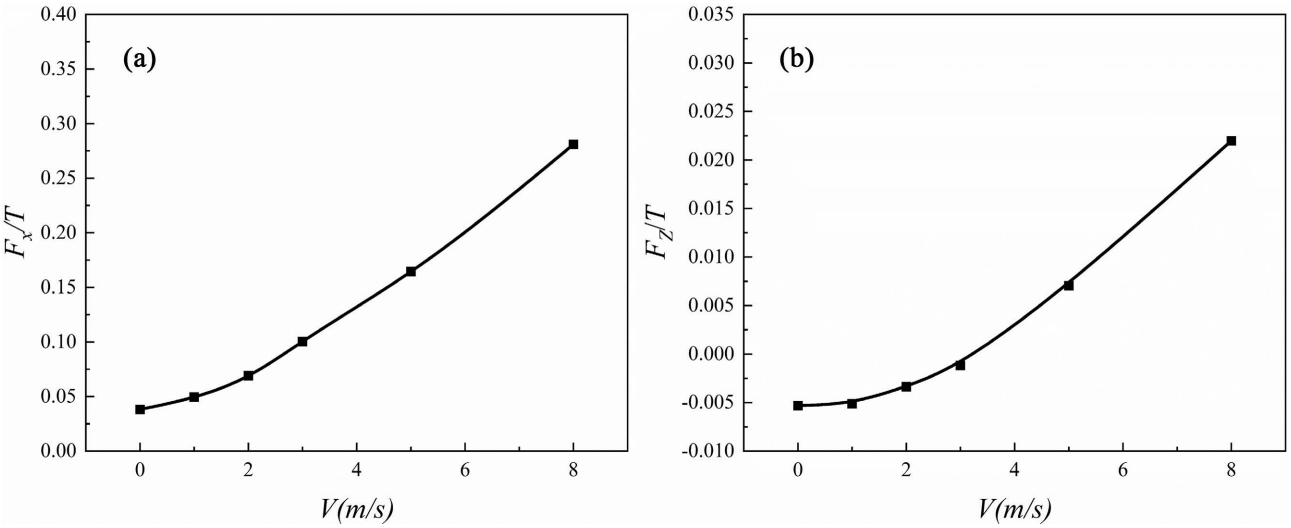


**Figure 8.** Variation of aerodynamic loads on the wing during the transition (tilt) phase with changing freestream conditions. (a) Variation of $F_x/T$ with with V; (b) Variation of $F_z/T$ with with V.

above analysis, the subsequent sections of this chapter focus primarily on the effects of the horizontal force $F_x$ acting on the tilt-segment wing.

As shown in Figure 9, the velocity slice contours are presented for inflow velocities of 3 m/s and 5 m/s. With the gradual increase in the inflow velocity, the overall velocity level of the rotor wake increases significantly. Influenced by the upstream freestream, the high-speed wake impinging on the right side of the tilt-transition wing is convected closer to the wing surface. The resulting asymmetric distributions of velocity and pressure gradients on the two sides of the wing generate a rearward horizontal force, $F_x$ acting on the tilt-transition wing.

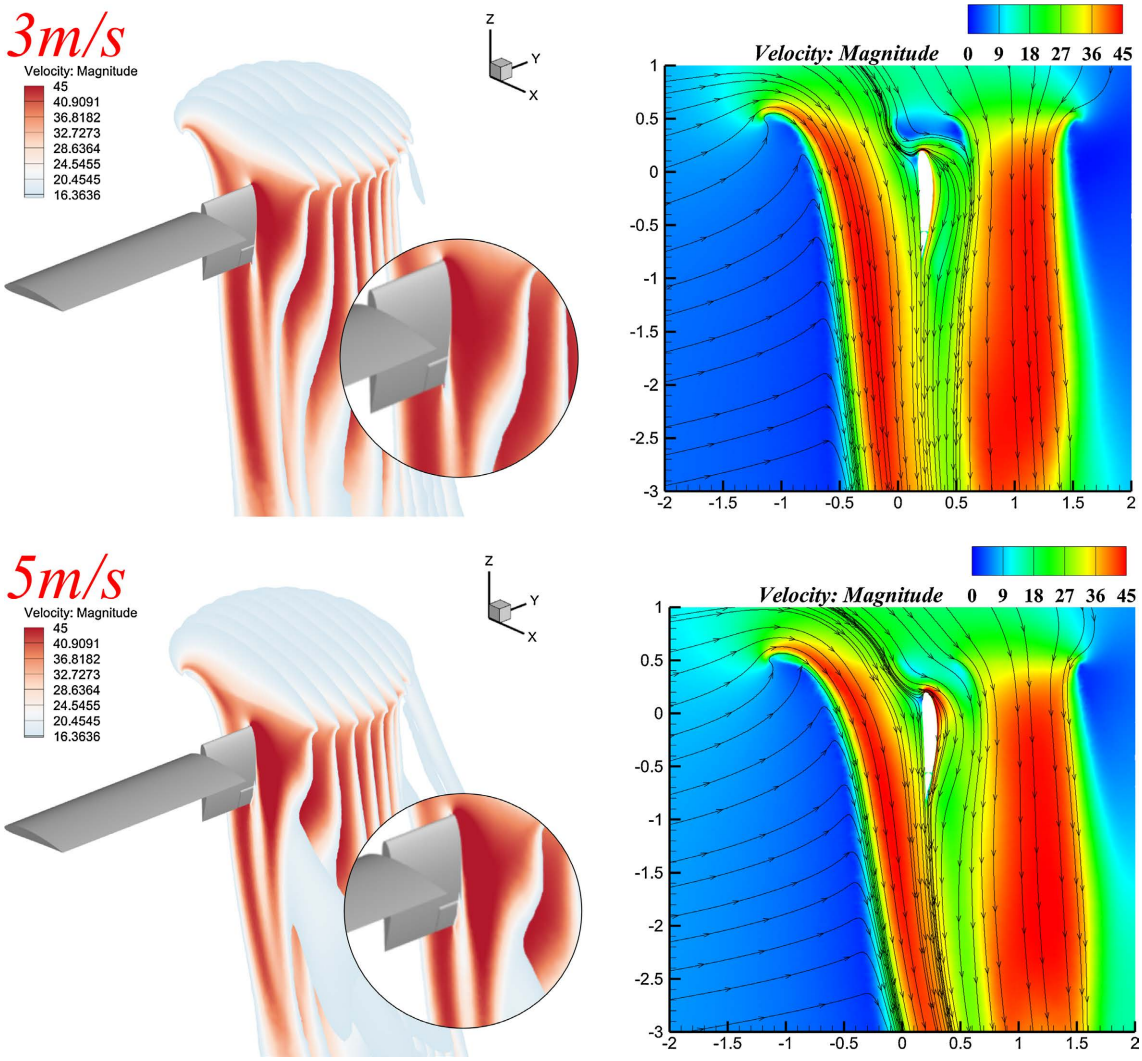


Figure 9. Velocity contour slices and corresponding velocity streamline cross-sections.

## 4. Study on the Aerodynamic Interference Characteristics of Rotor-Wing Interaction in the Tilt Phase with Continuous Flaperon Deflection

This subsection employs an unsteady numerical simulation approach to systematically investigate the aerodynamic interference of a tiltwing aircraft operating in

helicopter mode. By introducing a time scale, the unsteady computations are capable of more realistically capturing the temporal evolution of aerodynamic forces during control surface (flaperon) deflection.

In the present study, a continuously varying flaperon deflection angle is considered, and the unsteady Reynolds-averaged Navier-Stokes (URANS) method is adopted for the numerical simulations. The unsteady results are further compared with the steady-state solutions obtained in the previous subsection, thereby providing a more reliable theoretical basis for analyzing the aerodynamic response characteristics of tiltwing aircraft during the transition phase under dynamic operating conditions.

### 4.1. Computational Conditions

Under freestream velocities of 3 m/s and 5 m/s, unsteady numerical simulations were conducted to investigate the flaperon deflection process. The flaperon deflection angle was continuously varied from an initial 0˚ to −45˚. To examine the influence of different deflection rates on the aerodynamic interference between the wing and the rotor in the transition segment of a tilt-rotor configuration, the flaperon deflection durations were set to 0.5 s, 1 s, and 2 s, respectively. A constant angular deflection rate was maintained throughout the entire deflection process. The specific computational cases are summarized in Table 3.

Table 3. The flaperon deflection condition under unsteady calculation.

| Parameters | Value |
|---|---|
| Freestream velocity (m/s) | 3, 5 |
| Fixed-wing angle of attack(deg) | 0 |
| Rotor and tilt-wing segment angle (deg) | 86 |
| Rotor rotation speed (RPM) | 1500 |
| Flaperon deflection angle (deg) | 0 - −45 |
| Flaperon deflection completion time(s) | 0.5, 1 s, 2 s |

### 4.2. Computational Results

Figure 10 presents a comparison of the variations in $F_x/T$ with respect to the flaperon deflection angle, as computed using steady and unsteady methods under an incoming flow velocity of 3 m/s, for different flaperon deflection completion times. Overall, the unsteady results exhibit trends consistent with those obtained from the steady approach, with $F_x/T$ decreasing as the absolute value of the flaperon deflection angle increases.

When the flaperon deflection angle lies within the range of −20˚ to 0˚, the $F_x/T$ values predicted by different computational methods show only minor discrepancies. The results follow similar trends with respect to the deflection angle and display an approximately linear variation, indicating that within the small-deflection regime, the aerodynamic response is relatively insensitive to the choice of compu-

tational method and to unsteady effects. As the flaperon deflection angle further increases and enters the range of −20˚ to −45˚, $F_x/T$ transitions from positive to negative values, and noticeable differences begin to emerge among the results obtained using unsteady methods. In particular, for a deflection completion time of 0.5 s, $F_x/T$ exhibits a pronounced reduction near a deflection angle of approximately −25˚, yielding values significantly lower than those predicted by the steady computation as well as those corresponding to other deflection completion times.

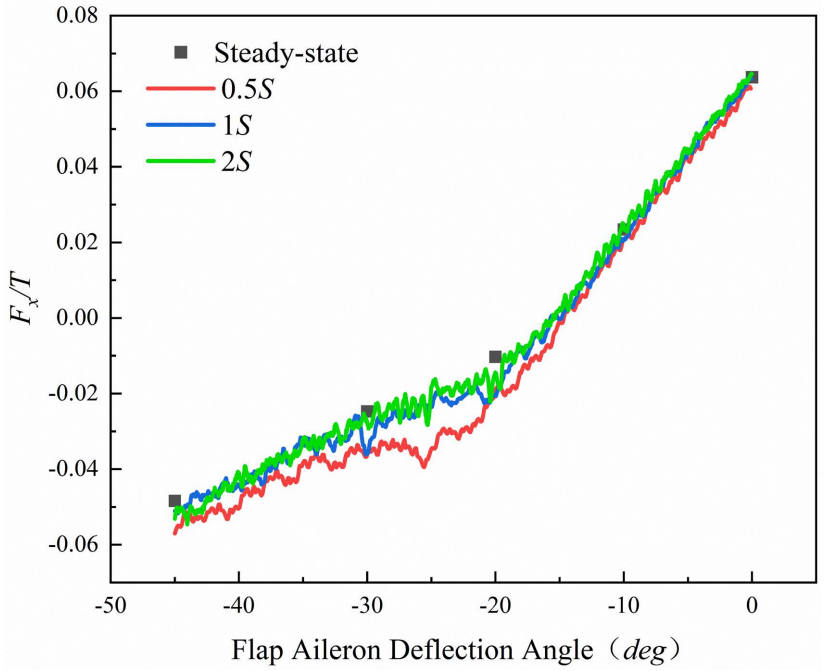


**Figure 10.** Variation of $F_x$/T with flaperon deflection angle under freestream velocities of 3 m/s.

Figure 11 presents a comparison of the variation of $F_x/T$ with the flaperon deflection angle obtained using different computational approaches at an inflow velocity of 5 m/s. In terms of both overall trend and magnitude, the unsteady simulation results are in good agreement with those from the steady-state calculations. Specifically, $F_x/T$ decreases monotonically as the absolute value of the flaperon deflection angle increases.

The $F_x/T$ results obtained using different computational approaches exhibit noticeable quantitative discrepancies, which are primarily concentrated in the flaperon deflection angle range of −20˚ to −45˚. Within this deflection interval, the $F_x/T$ values predicted by the steady-state computations are generally slightly higher than those obtained from the unsteady simulations. The overall variation trend is consistent with that observed at an inflow velocity of 3 m/s. Further comparison of the results corresponding to different deflection completion times indicates that, near a deflection angle of approximately −25˚, the unsteady simulation with a deflection completion time of 0.5 s yields a markedly lower $F_x/T$ value than both the steady-state result and the unsteady results associated with other deflection

completion times. This behavior is similar to that observed under the 3 m/s inflow condition. A detailed analysis focusing on this specific deflection angle is presented in the subsequent sections.

Given that the overall variation trends of $F_x/T$ with respect to flaperon deflection angle are essentially consistent for inflow velocities of 3 m/s and 5 m/s, and considering that the unsteady aerodynamic force fluctuations are relatively smaller and the flow exhibits higher stability at an inflow velocity of 5 m/s, the 5 m/s condition is selected as a representative case for subsequent investigations of flow-field structural characteristics. Figure 12 illustrates the Q-criterion-based vortex structure distribution of the overall tilt-wing flow field, where a Q-criterion

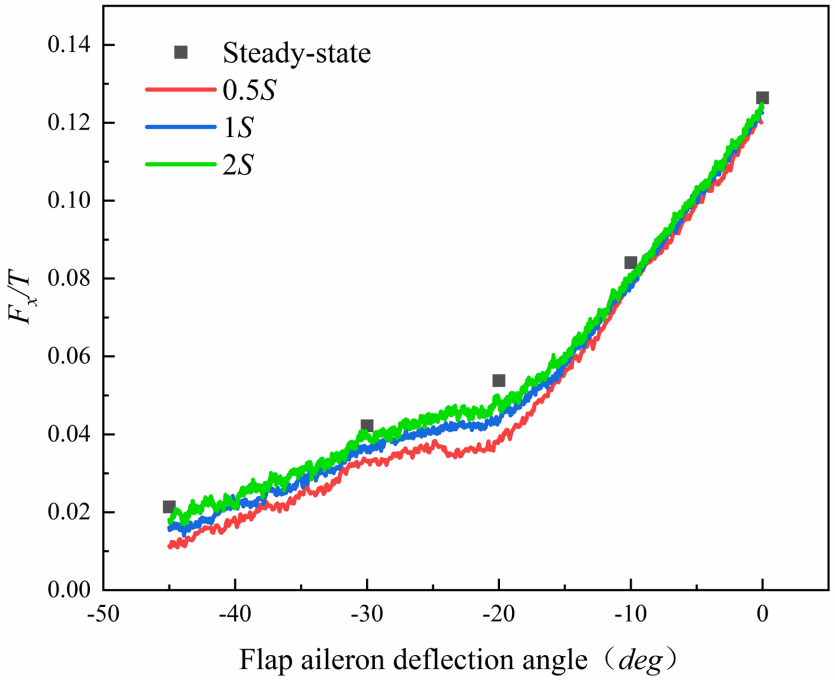


Figure 11. Variation of $F_x$/T with flaperon deflection angle under freestream velocities of 5 m/s.

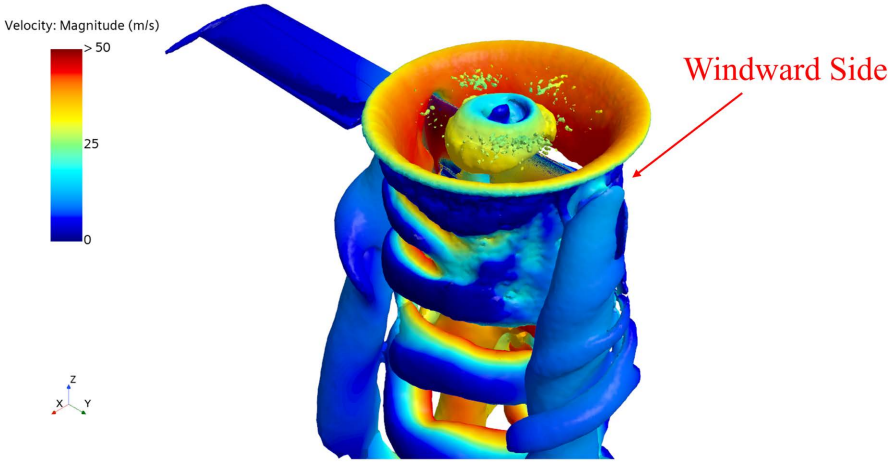


Figure 12. Overall vortex distribution of tilt-wing.

threshold of 1500 $s^{-2}$ is adopted to identify and characterize the dominant vortical structures.

The spiral vortex structure observed in the low-velocity region at the center of the virtual disk is essentially an equivalent representation of the hub vortex reproduced by the virtual disk model under the condition of an "absence of a physical hub." In practical propeller or rotor systems, a concentrated axial vortex structure is generated downstream of the hub as a result of the combined effects of boundary-layer separation on the hub surface and the pronounced circumferential velocity shear within the rotating wake. The vortex core of the hub vortex is characterized by distinct low-pressure and low-velocity features and develops helically in the downstream direction. Its influence may extend to the wing surfaces on both sides of the tilt-transition section, where local attachment can occur.

When the flaperon begins to deflect, the aerodynamic characteristics of the control surface undergo significant changes. As the deflection angle increases progressively, the adverse pressure gradient on the lower surface of the flaperon intensifies, leading to boundary-layer separation and the formation of a pronounced separation vortex. During its development, this separation vortex interacts and couples with the upstream hub vortex, thereby further modifying the local flowfield structure. Figure 13 presents the velocity streamline distribution for a flaperon deflection angle of −22.5˚ with a deflection completion time of 2 s, where a distinct and finite-scale separation vortex can be clearly identified beneath the flaperon.

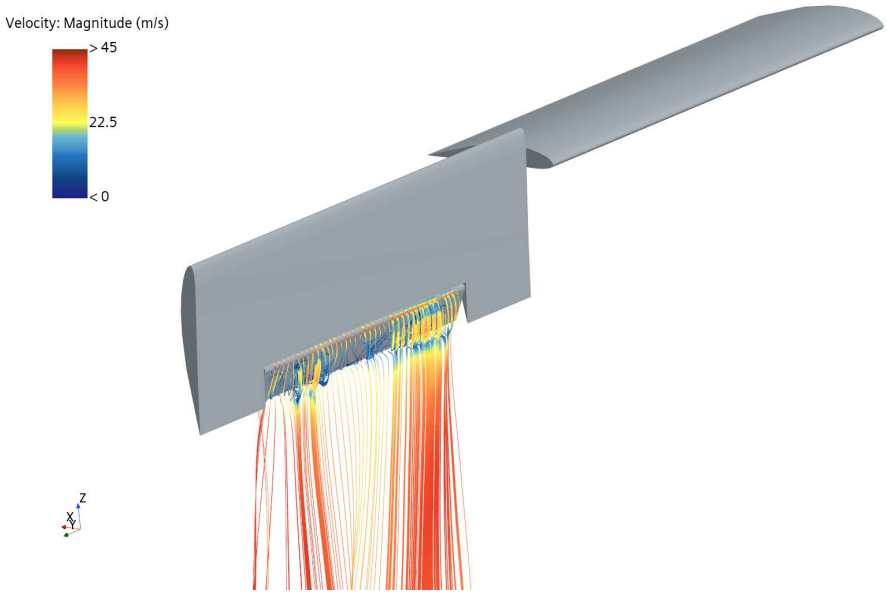


Figure 13. Velocity streamline plot at −22.5˚ flaperon deflection.

Different flaperon deflection rates have a pronounced influence on the evolution of the propeller hub vortex. Under different inflow conditions, the aerodynamic loads exhibit an overall consistent trend with respect to the flaperon deflection angle. In the present study, the case with an inflow velocity of 5 m/s is selected

for detailed analysis. Figure 14 presents vortex structure contours on the windward side of the tilting-wing segment for flaperon deflection completion times of 0.5 s, 1 s, and 2 s, all with a deflection angle of 22.5˚. As shown in the figure, the overall vortex system becomes increasingly stable with longer deflection completion times. When the flaperon deflection completion time reaches 2 s, the separation vortex generated on the flaperon couples with the propeller hub vortex, resulting in a more coherent and stable vortex structure.

Figure 15 presents vortex-structure contours on the windward surface of the tilting wing on the leeward side for flaperon deflection completion times of 0.5 s, 1 s, and 2 s, with a constant deflection angle of −22.5˚. The propeller hub vortex initially forms a columnar helical vortex convecting downstream along the propeller axis. As it passes over the upper surface of the flaperon, the imposed flaperon deflection forces the root vortex filament to follow the increasingly curved wing surface, thereby reducing the distance between the vortex core and the wall and intensifying wall confinement effects. The abrupt increase in trailing-edge camber

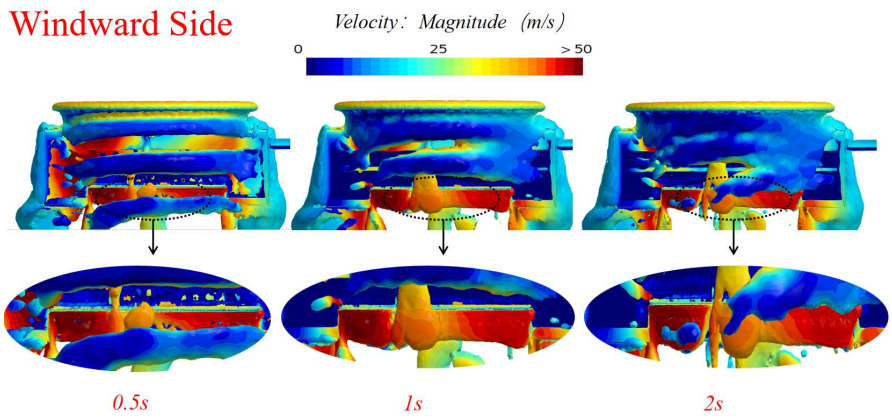


Figure 14. Vortex distribution on the windward side of the tilt-wing segment under different deflection completion times.

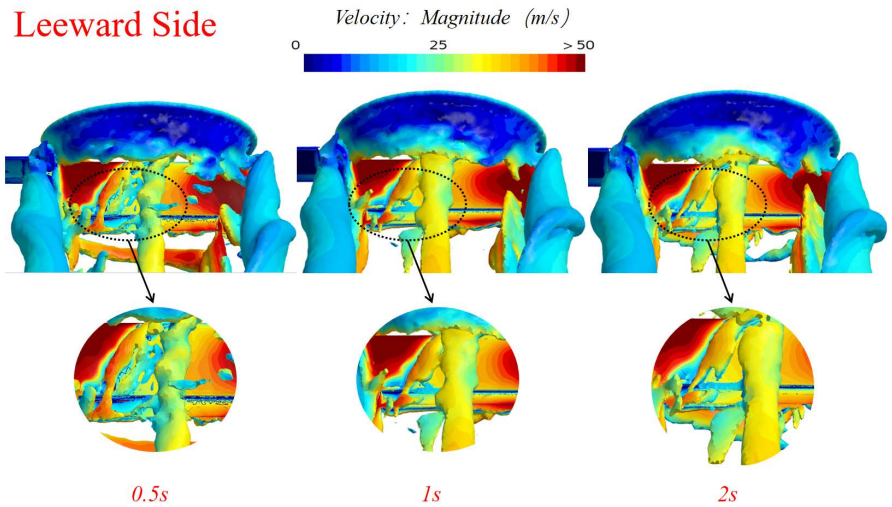


Figure 15. Vortex distribution on the leeward side of the tilt-wing segment under different deflection completion times.

subjects the hub vortex to an adverse pressure gradient, under which it progressively destabilizes and disintegrates. In the contour plots, this process is manifested as a sudden interruption of the vortex structure accompanied by a rapid transition in the color scale. As the deflection completion time increases from 0.5 s to 2 s, the hub vortex remains more coherent and exhibits a more stable core.

Figure 16 presents contour plots of the surface pressure coefficient distribution on the leeward side of the wing during the transition phase, for flapleron deflection completion times of 0.5 s, 1 s, and 2 s, all with a deflection angle of −22.5˚. The integrity of the vortex system exhibits a strong correspondence with the surface low-pressure regions: the more stable the vortex core, the lower the resulting surface pressure. The degree of near-wall attachment of the hub vortex emerges as a key factor accounting for the discrepancies between the local pressure distribution and the horizontal force response.

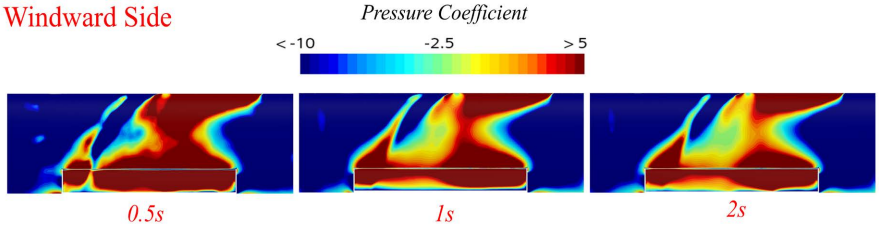


Figure 16. Surface pressure coefficient contour plots of the tilt-wing segment under different deflection completion times.

**Key Weaknesses:**

Geometric Simplification: The model is highly simplified, utilizing a rectangular straight wing and neglecting the fuselage, horizontal tail, and lateral-directional forces. While this isolates the rotor-wing interaction, it may limit the applicability of the results to real-world aircraft configurations where these interactions are significant.

## 5. Conclusions

Based on a mesh reconstruction technique, the present study simulates the flaperon deflection process and establishes a numerical methodology capable of effectively modeling flaperon deflection in the helicopter mode of a tiltwing aircraft. A comparative analysis is conducted between unsteady simulations with continuous flaperon deflection and steady-state simulations with fixed flaperon deflection angles. The main conclusions are summarized as follows:

- The variation trends of aerodynamic forces acting on the wing with respect to flaperon deflection angle obtained from unsteady and steady simulations are generally consistent.
- Unsteady simulation results indicate that the flaperon deflection rate has a significant influence on the formation, evolution, and stability of hub vortices. Excessively high deflection rates may lead to vortex breakdown and anomalous pressure distributions, thereby degrading the effectiveness of flaperon deflec-

tion. Consequently, an appropriate deflection rate should be selected in practical control applications.

## Funding

This work was supported by National Natural Science Foundation of China (12362026), Nanchang University of Aeronautics and Astronautics Graduate Student Innovation Special Funds Programme (Provincial-Level Project: YC2024-S624).

## Conflicts of Interest

The authors declare no conflicts of interest regarding the publication of this paper.

## References

[1] Jia, Y.N. (2025) Preliminary Study on Traffic Management Schemes for Unmanned Systems in Low-Altitude Airspace. *Acta Aeronautica et Astronautica Sinica*, **46**, 121-147.

[2] Wu, A.B., Wang, Z. and Li, R. (2025) Operational Scenarios and Key Technologies of eVTOL Unmanned Aerial Vehicles in Urban Low-Altitude Airspace. *Electro-Optic and Control*, **32**, 1-7.

[3] Chen, Y., Liu, L. and Zeng, Y.H. (2010) Key Technologies for the Future Development of Unmanned Systems in the U.S. Military. *Aerodynamic Missile Journal*, No. 7, 33-37.

[4] Prevot, T., Smith, N.M., Palmer, E., Callantine, T.J., Lee, P.U., Mercer, J., Martin, L., Brasil, C. and Cabrall, C.D. (2014) An Overview of Current Capabilities and Research Activities in the Airspace Operations Laboratory at NASA Ames Research Center. *14th AIAA Aviation Technology, Integration, and Operations Conference*, Atlanta, 16-20 June 2014. https://doi.org/10.2514/6.2014-2860

[5] Straubinger, A., Rothfeld, R., Shamiyeh, M., Büchter, K., Kaiser, J. and Plötner, K.O. (2020) An Overview of Current Research and Developments in Urban Air Mobility—Setting the Scene for UAM Introduction. *Journal of Air Transport Management*, **87**, Article ID: 101852. https://doi.org/10.1016/j.jairtraman.2020.101852

[6] Coppola, P., De Fabiis, F. and Silvestri, F. (2024) Urban Air Mobility (UAM): Airport Shuttles or City-Taxis? *Transport Policy*, **150**, 24-34. https://doi.org/10.1016/j.tranpol.2024.03.003

[7] Bacchini, A. and Cestino, E. (2019) Electric VTOL Configurations Comparison. *Aerospace*, **6**, Article 26. https://doi.org/10.3390/aerospace6030026

[8] Ugwueze, O., Stühteros, T., Bromfield, M. and Horri, N. (2023) Trends in eVTOL Aircraft Development: The Concepts, Enablers and Challenges. *AIAA SCITECH* 2023 *Forum*, National Harbor, 23-27 January 2023. https://doi.org/10.2514/6.2023-2096

[9] Deng, J.H. (2024) Technical Status and Development of Electric Vertical Take-Off and Landing Aircraft. *Acta Aeronautica et Astronautica Sinica*, **45**, Article ID: 529937.

[10] Misra, A., Jayachandran, S., Kenche, S., Katoch, A., Suresh, A., Gundabattini, E., *et al.* (2022) A Review on Vertical Take-Off and Landing (VTOL) Tilt-Rotor and Tilt Wing Unmanned Aerial Vehicles (UAVs). *Journal of Engineering*, **2022**, Article ID: 1803638. https://doi.org/10.1155/2022/1803638

[11] Maisel, M. and Harris, D. (1981) Hover Tests of the XV-15 Tilt Rotor Research Air-

craft. 1*st Flight Test Conference*, Las Vegas, 11 November-13 November 1981, p. 15. https://doi.org/10.2514/6.1981-2501

[12] Felker, F.F. and Light, J.S. (1988) Aerodynamic Interactions between a Rotor and Wing in Hover. *Journal of the American Helicopter Society*, **33**, 53-61. https://doi.org/10.4050/jahs.33.53

[13] Li, P. and Zhao, Q.J. (2016) CFD Analyses of Aerodynamic Characteristics of Tiltrotor under Typical Flight Conditions. *Journal of Aerospace Power*, **31**, 421-431.

[14] Wang, Z.H., Yang, Y.J., Zhao, H.R. and Zhao, J.X. (2024) Numerical Simulation of Tilting Wing and Rotor UAV during Transition Flight. *Modern Defence Technology*, **52**, 9-19.

[15] Liu, J.H., Li, G.H. and Wang, F.X. (2022) Rotor-Wing Aerodynamic Interference Characteristics in Conversion Mode. *Acta Aeronautica et Astronautica Sinica*, **43**, 214-225.

[16] Shi, J.S., Fang, X., Zhang, X.Y., Zhao, G.Q. and Wang, B. (2023) Influence of Flight Speed in Transition State on Aerodynamic Performance of Tiltrotor Aircraft. *Flight Dynamics*, **41**, 1-6.

[17] Li, P., Zhao, Q.J., Wang, Z.Z. and Wang, B. (2015) Highly-Efficient CFD Method for Predicting Aerodynamic Force of Tiltrotor in Conversion Mode. *Journal of Nanjing University of Aeronautics & Astronautics*, **47**, 189-197.

[18] Wang, Y.C. He, G.Y. and Wang, Q. (2022) Aerodynamic Performance Analysis and Optimization of Tiltwing UAV in Return Transition Section. *Science Technology and Engineering*, **22**, 9848-9856.